INTERNATIONAL JOURNAL FOR NUMERICAL METHODS IN FLUIDS
Int. J. Numer. Meth. Fluids 2005; **47**:871–877
Published online 4 January 2005 in Wiley InterScience (www.interscience.wiley.com). DOI: 10.1002/fld.880

Chaotic mixing in a basin due to a sinusoidal wind field

Qiuhua Liang, Alistair G. L. Borthwick*,† and Paul H. Taylor

Department of Engineering Science, University of Oxford, Parks Road, Oxford OX1 3PJ, U.K.

SUMMARY

This paper presents a novel numerical study of wind-induced mixing in a circular shallow lake. The wind-induced hydrodynamic field is first predicted by a Godunov-type shallow water equation solver based on a quadtree grid. Then the horizontal mixing processes are analysed in terms of chaotic advection. The particle dynamics under a sinusoidal wind field are found to change from regular to chaotic states with increasing period of wind oscillation. The numerical approach is applicable to a wide range of environmental flows. Copyright © 2005 John Wiley & Sons, Ltd.

KEY WORDS: chaotic advection; quadtree grid; shallow water equations

1. INTRODUCTION

Mixing in shallow flows is an important topic in environmental engineering. Relevant examples include pollutant dispersion, the movement of suspended sediment in rivers and coastal waters, the spread of algal blooms in lakes, and the wind-induced transport of suspended mine material in tailings ponds. These processes directly affect water quality, and can have significant impacts on the ecosystem [1].

Mixing in fluid flows can be conveniently analysed by considering particle advection. In a seminal paper, Aref [2] investigated particle motions induced by a repeatedly blinking vortex flow and found that passive tracers could follow chaotic paths and so greatly enhance mixing in simple unsteady flows. Since then, there has been an intensive research campaign to study chaotic advection by tracking particles [3–5]. Herein we intend to study chaotic mixing using numerically simulated flow fields with the aim of applying the model eventually to shallow environmental flows.

The case we shall consider is that of wind-induced mixing in a circular shallow basin, originally proposed by Kranenburg [4]. Using an alternating wind field of constant intensity,

*Correspondence to: Alistair G. L. Borthwick, Department of Engineering Science, University of Oxford, Parks Road, Oxford OX1 3PJ, U.K.
†E-mail: alistair.borthwick@eng.ox.ac.uk

Contract/grant sponsor: U.K. EPSRC; contract/grant number: GR/R13623

Received 27 April 2004
Revised 1 September 2004
Accepted 22 September 2004

Kranenburg found that the oscillatory wind-induced circulation patterns could cause the particle motions to become chaotic. Kranenburg approximated the depth-integrated hydrodynamics by means of a simplified analytical solution of the governing momentum equations. In practice, however, an idealized analytical velocity field is not available for natural shallow water flows, where the bed topographies and flow patterns are usually very complicated. Therefore, in this paper numerical schemes are proposed to tackle the problem, and the wind field is assumed to be sinusoidally changing both in direction and intensity so that it is more suited to realistic cases.

2. HYDRODYNAMICS

Consider a circular basin of axi-symmetric bathymetry, with the still water depth h_s given by the following formula [4]:

$$h_s = H\left(\frac{1}{2} + \left(\frac{1}{2} - \frac{1}{2}\frac{r}{R_0}\right)^{1/2}\right) \tag{1}$$

where $H = 0.5\,\mathrm{m}$ is a weighted mean water depth, r is the distance from the basin centre, and $R_0 = 120\,\mathrm{m}$ is the radius of the circular basin. The top view and cross-section of the basin are illustrated in Figure 1. The water is initially at rest and subject to a sinusoidally changing wind field after $t = 0$. Wind stresses are applied everywhere on the water surface with the wind direction θ and intensity τ_w changing sinusoidally:

$$\begin{aligned}
&\theta = \theta_1 + (\theta_2 - \theta_1)\sin\left(\frac{\hat{t}}{t_s}\frac{\pi}{2}\right), \quad \tau_w = A_w \sin\left(\frac{\hat{t}}{t_s}\pi\right), \quad \text{when } \hat{t} \leqslant t_s \\
&\theta = \theta_2 - (\theta_2 - \theta_1)\sin\left(\frac{\hat{t} - t_s}{t_s}\frac{\pi}{2}\right), \quad \tau_w = A_w \sin\left(\frac{\hat{t} - t_s}{t_s}\pi\right), \quad \text{when } \hat{t} > t_s
\end{aligned} \tag{2}$$

Herein $\theta_1 = 45°$ and $\theta_2 = 135°$; $\hat{t} = [t \bmod T]$ with t denoting time and T being the period of the wind field; $A_w = 0.002\,\mathrm{N/m^2}$ is the amplitude of the wind stress; $t_s = T/2$.

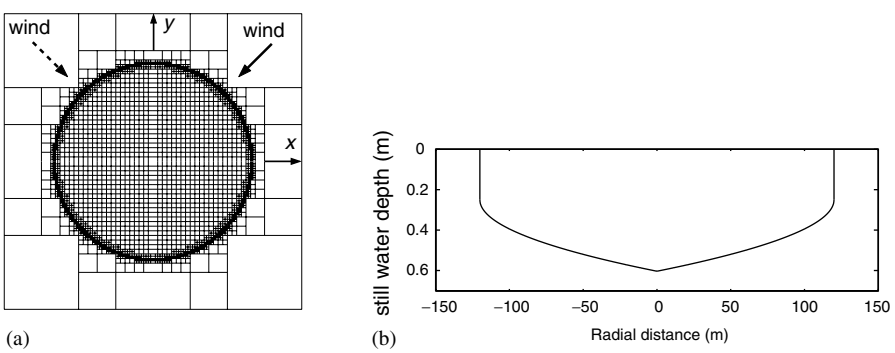

Figure 1. Basin geometry: (a) plan view (represented using a quadtree grid); and (b) cross-section described by Equation (1).

The hydrodynamics of the flow can be approximated by the shallow water equations which can be written in differential hyperbolic conservation form as [6]

$$\frac{\partial \mathbf{u}}{\partial t} + \frac{\partial \mathbf{f}}{\partial x} + \frac{\partial \mathbf{g}}{\partial y} = \mathbf{s} \tag{3}$$

where $\mathbf{u}$ is the vector of conserved variables, $\mathbf{f}$ and $\mathbf{g}$ are flux vectors, $\mathbf{s}$ is the vector of source terms, and x and y are Cartesian co-ordinates. Briefly,

$$\mathbf{u} = \begin{bmatrix} \zeta \\ uh \\ vh \end{bmatrix}, \quad \mathbf{f} = \begin{bmatrix} uh \\ u^2h + g(\zeta^2 + 2\zeta h_s)/2 - \varepsilon h \partial u/\partial x \\ uvh - \varepsilon h \partial v/\partial x \end{bmatrix}$$
$$\mathbf{g} = \begin{bmatrix} vh \\ uvh - \varepsilon h \partial u/\partial y \\ v^2h + g(\zeta^2 + 2\zeta h_s)/2 - \varepsilon h \partial v/\partial y \end{bmatrix}, \quad \mathbf{s} = \begin{bmatrix} 0 \\ (\tau_{wx} - \tau_{bx})/\rho - g\zeta S_{ox} + hfv \\ (\tau_{wy} - \tau_{by})/\rho - g\zeta S_{oy} - hfu \end{bmatrix} \tag{4}$$

where ζ is the water surface elevation above still water level (h_s); h ($=h_s + \zeta$) is the total water depth; u and v are the depth-averaged velocity components in the x- and y-directions, respectively; ε is the depth-averaged kinematic eddy viscosity coefficient; f is the Coriolis parameter and is ignored here; $g = 9.81\ \mathrm{m/s^2}$ is the acceleration due to gravity; $\rho = 1000\ \mathrm{kg/m^3}$ is water density; $\tau_{wx} = \tau_w \cos(\theta)$ and $\tau_{wy} = \tau_w \sin(\theta)$ are the surface (wind) stress components in two co-ordinate directions; τ_{bx} and τ_{by} are the bed friction stresses; S_{ox} ($=-\partial h_s/\partial x$) and S_{oy} ($=-\partial h_s/\partial y$) are the bed slopes and can be obtained by partially differentiating Equation (1). The above shallow water equations mathematically balance the flux gradient and source terms [6].

The shallow water equations are solved using a quadtree grid-based finite volume Godunov-type numerical scheme, implemented with the HLLC approximate Riemann solver and second-order MUSCL-Hancock method [7]. The circular basin is approximated by a quadtree grid as shown in Figure 1(a), where the co-ordinate system is illustrated in the same graph. The quadtree grid has highest and lowest subdivision levels of 8 and 6, respectively, indicating that a maximum ratio of cell size is $2^8/2^6$. The grid has a total of 2796 leaf cells. The water is initially at rest and the bed stress terms are evaluated empirically using

$$\tau_{bx} = \rho C_f u \sqrt{u^2 + v^2} \quad \text{and} \quad \tau_{by} = \rho C_f v \sqrt{u^2 + v^2} \tag{5}$$

in which the bed roughness coefficient C_f for calculating bed stresses is estimated by [9]

$$C_f = \left[\frac{\kappa}{1 + \ln(z_0/h)} \right]^2 \tag{6}$$

where $\kappa = 0.4$ is the von Karman constant, $z_0 = 2.8$ mm is the roughness height of the bed. A depth-averaged eddy viscosity coefficient is evaluated via $\varepsilon = \kappa u_* h/6$ with $u_* = \sqrt{A_w/\rho}$ being the friction velocity at the free surface. Slip conditions are imposed at the circular boundary so that no flux goes through the boundary in the radial direction. A fixed time step of $\Delta t = 0.5$ s is used. After an initial transient phase, the flow pattern consists of a pair of topographic gyres that oscillate in position throughout the wind cycle, for all cases

considered. For tracking purposes, instantaneous velocity fields are stored over a cycle using singular value decomposition (SVD) [8] with 8 modes, retaining $>99\%$ of the variance.

3. WIND-INDUCED ADVECTION

Having obtained the wind-induced Eulerian velocity field, tracer particles are moved by time-integration of the advection equations using a fourth-order Runge–Kutta algorithm, which permits relatively large time steps and is suitable for application with dynamically adaptive grids. The algorithm is more accurate in time than space because the particle motions are very complicated temporally, even though the velocity field is always smooth in space. The continuous form of the velocity field is constructed using bilinear interpolation. In a 2-D Cartesian co-ordinate system, the advection equations are

$$\frac{\mathrm{d}x}{\mathrm{d}t} = u(x, y, t), \quad \frac{\mathrm{d}y}{\mathrm{d}t} = v(x, y, t) \tag{7}$$

where (x, y) is the position of a given particle at time t; and u and v denote the Eulerian velocity components in the x- and y-directions of the flow at the same spatial and temporal point as the particle.

The flows under consideration form weak systems, i.e. the chaotic motion increases as the perturbation becomes stronger. A single parameter related to the storm duration t_s (the wind event in one period T consists of two storms t_s) can be used to govern the system. After spatial non-dimensionalization with respect to the radius of the circular basin R_0 and introducing the dimensionless time variable $\tilde{t} = \ln(Z)u_* t/(8\kappa R_0)$, Kranenburg's dimensionless storm duration parameter (that governs the system) is defined as [4]

$$\mu = \frac{\ln(H/z_0)}{8\kappa} \frac{u_* t_s}{R_0} \tag{8}$$

Interpretation of the wind-induced advection begins by examining Poincaré sections that are produced by plotting the intersections of the particle trajectories with the time plane at the end of each period (Figure 2). For this purpose 10 particle tracers are released along the x-axis ($y = 0$) and tracked for up to 250 periods for different μ. For small μ (such

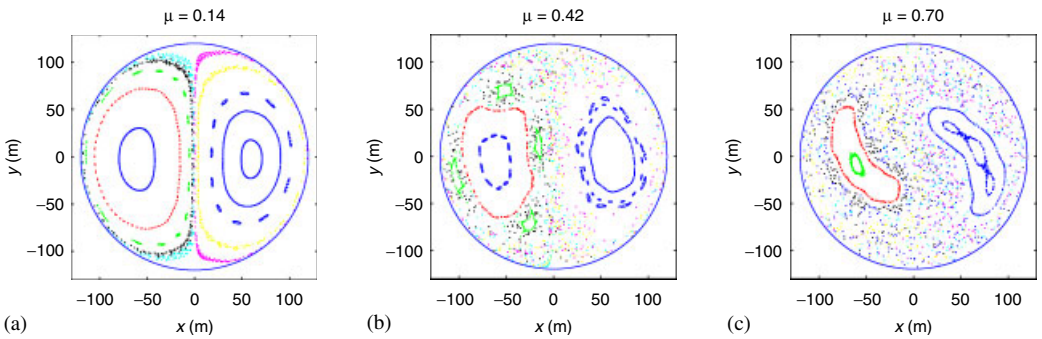

Figure 2. Poincaré sections corresponding to different μ.

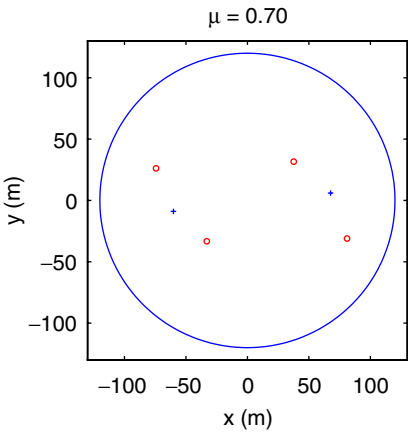

Figure 3. Periodic elliptic points for a flow with $\mu = 0.70$ (+: period-one; ○: period-two).

as 0.14), the Poincaré sections form two large period-one islands and different types of particle motion coexist. The period-one islands, characterized by regular particle motions, lie on both sides of the north-south axis and each surrounds a period-one elliptic point. Chains of smaller scale islands surround the regular regions. Outside the island chains, the particle motions are about to become chaotic near the north-south axis and basin perimeter. As μ increases (e.g. $\mu = 0.42$), the period-one islands shrink in size and the particle trajectories become more and more chaotic. When μ is further increased to 0.70, both period-one islands greatly reduce in size and stretch and shrink in two different directions, indicating that the corresponding period-one elliptic points are changing to hyperbolic points. At approximately $\mu = 0.84$, all the low-order periodic islands have disappeared and the advection of particles has reached a globally chaotic stage. Our Poincaré sections agree with those obtained using the analytical velocity field suggested by Kranenburg [4]. It should be noted that particles attempting to cross the perimeter of the domain are reflected back into the interior. This inevitably introduces additional error into the calculation of particle trajectories. However, since the particle motions near the boundary are invariably chaotic for large values of μ, the scheme provides a proper qualitative description of particle dynamics.

The properties of periodic fixed points determine the dynamics of nearby particles and the main obstacle to mixing arises from island-type structures corresponding to low-order periodic elliptic points. Herein the periodic points inside the basin can be detected using the Schmelcher–Diakonos (SD) method [10]. The SD method has global convergence properties and does not need *a priori* knowledge about the system. Most of the periodic fixed points can be detected by using a finite number of initial points. Here 40 initial points are used and the results are unchanged if more (up to 716) points are used. Low-order periodic elliptic points (of periods T or $2T$) with visible island structures are to be stabilized for $\mu = 0.70$ and 0.84. Figure 3 shows the periodic elliptic points detected for $\mu = 0.70$, which are consistent with the corresponding Poincaré sections. Once an elliptic point has been detected, we calculate the surrounding island structure by producing the Poincaré sections for a particle tracer at a prescribed distance D from that point. The maximum size of the island is estimated by slowly increasing D. For the six low-order periodic elliptic points shown in Figure 3, the maximum

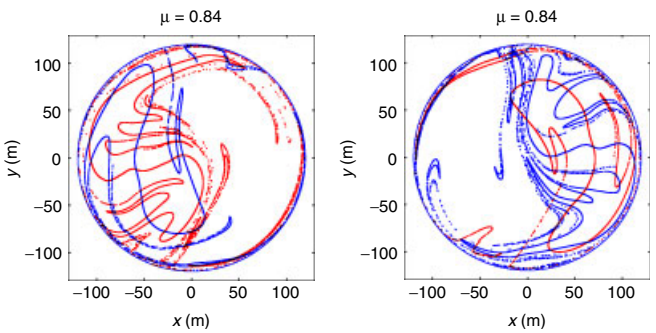

Figure 4. Stable (blue) and unstable (red) manifolds corresponding to the period-one hyperbolic points for $\mu = 0.84$.

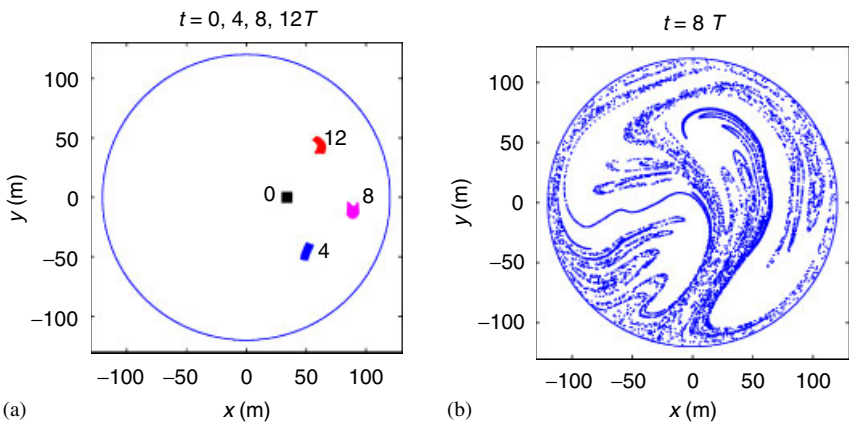

Figure 5. Advection of a square particle patch: (a) $\mu = 0.28$; and (b) $\mu = 0.84$

value for D is about 7 m. At $\mu = 0.84$, no periodic elliptic points of periods T or $2T$ are found, which indicates that all the low-order periodic points have changed to hyperbolic. Two period-one hyperbolic points are located at about $(69, 11)$ and $(-58, -12)$. Parts of the corresponding stable and unstable manifolds are shown in Figure 4. These complicated manifolds contribute to the chaotic behaviour of the particle tracers. Therefore no large-scale island structure survives for $\mu = 0.84$, and the flow is well-mixed.

Particles inside different regions of the flow undergo different mixing processes, which can be visualized by tracing the fate of a particle patch. Consider a square array containing 10 000 particles with side length of 8 m. Figure 5(a) records snapshots of the square particle patch inside the eastern period-one island for $\mu = 0.28$ at $t = 0$, 4, 8, $12T$. As the patch wanders inside the island its original shape slowly deforms, indicating regular particle behaviour in the region. Figure 5(b) presents the evolution of a square particle patch released into the flow near the lower boundary with $\mu = 0.84$. The small particle patch has developed into a very complicated filament structure after 8 periods. The influence of the unstable manifolds corresponding to the two period-one hyperbolic points on the structure is evident. By increasing

the simulation time, more and more complicated structures develop until the whole basin is filled by tracks.

4. CONCLUSIONS

A numerical approach for investigating wind-induced chaotic mixing in a circular shallow basin has been described, with the hydrodynamics of the flow predicted by a robust quadtree-based Godunov-type shallow water equation solver and mixing analysed via particle tracking. Under a sinusoidal changing wind field, tracer particle motions are found to change from regular to chaotic as the wind period increases. The model is applicable to studying qualitatively mixing processes in natural lakes. It should be noted, however, that the model is limited by its assumptions of two-dimensional hydrostatic flow. For complete predictions of wind-driven particle dynamics in enclosed basins, a three-dimensional model is necessary [1].

ACKNOWLEDGEMENTS

The U.K. EPSRC has supported this work under Grant GR/R13623. Part of the computation has been carried out in the Oxford Supercomputing Centre.

REFERENCES

1. Colombini M, Stocchino A. 3D transport of a passive pollutant for wind-driven flows in enclosed basins. *Proceedings of International Symposium on Shallow Flows*, 16–18 June 2003, Delft University of Technology, The Netherlands.
2. Aref H. Stirring by chaotic advection. *Journal of Fluid Mechanics* 1984; **143**:1–21.
3. Ottino JM. *The Kinematics of Mixing*: *Stretching*, *Chaos*, *and Transport*. Cambridge University Press: Cambridge, 1989.
4. Kranenburg C. Wind-driven chaotic advection in a shallow model lake. *Journal of Hydraulic Research* 1992; **30**(1):29–46.
5. Károlyi G, Tél T. Chaotic tracer scattering and fractal basin boundaries in a blinking vortex-sink system. *Physics Reports* 1997; **290**:125–147.
6. Rogers BD, Borthwick AGL, Taylor PH. Mathematical balancing of flux gradient and source terms prior to using Roe's approximate Riemann solver. *Journal of Computational Physics* 2003; **192**(2):422–451.
7. Liang Q, Borthwick AGL, Stelling G. Simulation of dam- and dyke-break hydrodynamics on dynamically adaptive quadtree grids. *International Journal for Numerical Methods in Fluids* 2004; **46**:127–162.
8. Wunsch C. *The Ocean Circulation Inverse Problem*. Cambridge University Press: Cambridge, 1996.
9. Soulsby R. *Dynamics of Marine Sands*. Thomas Telford: Springfield, 1997.
10. Schmelcher P, Diakonos FK. General approach to the localization of unstable periodic orbits in chaotic dynamical systems. *Physical Review E* 1998; **57**(3):2739–2746.

